Rare Met. (2025) 44(8):5656–5671
https://doi.org/10.1007/s12598-025-03387-8

RARE METALS

ORIGINAL ARTICLE

Effects of PHB and PLA coatings on the corrosion behavior of ultrathin Mg sheets in artificial blood plasma containing BSA

Bi-Wei Sun, Ju-Yi Yang, Jian-Wei Dai, Yan-Bin Zhao, Lu Zhang, Zi-Jian Huang, Jing Bai, Feng Xue, Paul K. Chu, Cheng-Lin Chu*

Received: 27 December 2024 / Revised: 6 April 2025 / Accepted: 8 April 2025 / Published online: 24 June 2025

Abstract Biodegradable polymer coatings are commonly used as protective barriers on magnesium (Mg) and its alloys. The properties of polymers, such as crystallinity and degradation properties, have a crucial impact on their corrosion resistance. In this work, polyhydroxybutyrate (PHB) coatings are deposited on Mg sheets with a thickness similar to that of cardiovascular stents to assess the degradation behavior, and poly-lactic acid (PLA)-coated Mg is also investigated to compare the structure–property-performance relationship. The hydrogen evolution volume (HEV) of the PHB-coated sample decreases by 30% after immersion in artificial blood plasma (AP) for 7 days, whereas the PLA-coated sample shows an increase of 154%. The PHB coating also shows excellent durability at a constant voltage, compared to severe rupture of the PLA coating. The degradation behavior of the coated-Mg samples is evaluated in AP solution containing different concentrations of the bovine serum albumin (BSA). Corrosion is inhibited as the protein concentration increases. The degradation rates of the Mg, PLA-coated Mg, and PHB-coated Mg decrease by 65%, 88%, and 75% for 5 g L^{-1} BSA, respectively. Our results reveal that higher crystallinity and less acidic degradation products give rise to better durability, while the acid self-catalytic effect leads to the failure of PLA. The protein-polymer interactions are determined and the empirical relationship of HEV is established.

Keywords Magnesium; Poly(3-hydroxybutyrate); Poly-lactic acid; Protein adsorption; Corrosion resistance

Bi-Wei Sun and Ju-Yi Yang have contributed equally to this work.

Supplementary Information The online version contains supplementary material available at https://doi.org/10.1007/s12598-025-03387-8.

B.-W. Sun, J.-Y. Yang, J.-W. Dai, Y.-B. Zhao, L. Zhang, Z.-J. Huang, J. Bai, F. Xue, C.-L. Chu*
School of Materials Science and Engineering, Southeast University, Nanjing 211189, China
e-mail: clchu@seu.edu.cn

B.-W. Sun, J.-Y. Yang, J.-W. Dai, Y.-B. Zhao, L. Zhang, Z.-J. Huang, J. Bai, F. Xue, C.-L. Chu
Jiangsu Key Laboratory for Advanced Metallic Materials, Southeast University, Nanjing 211189, China

J.-W. Dai
Jiangsu JITRI Surface Engineering Technology Research Institute, Taizhou 225309, China

J. Bai
Institute of Medical Devices (Suzhou), Southeast University, Suzhou 215163, China

P. K. Chu
Department of Physics, Department of Materials Science and Engineering, Department of Biomedical Engineering, City University of Hong Kong, Hong Kong 999077, China

1 Introduction

Percutaneous coronary intervention (PCI) with stent placement is the most effective and rapid medical process for vascular stenosis and occlusion [1]. However, the application of nonbiodegradable stents is limited by late thrombosis, inflammation, and restenosis [2, 3]. Therefore, biodegradable alloys, especially magnesium (Mg) alloys, are considered promising alternatives due to their natural degradability [4], moderate mechanical properties [5], and excellent biocompatibility [6–8]. Nevertheless, the rapid degradation of Mg under physiological conditions can lead to inflammation and premature service failure [9–11]. For

example, restenosis was been observed at prematurely degraded sites of "Magmaris" in the BIOSOLVE series of studies conducted between 2013 and 2016 [12]. Therefore, the precise control of Mg degradation is crucial to the clinical adoption of Mg-based stents.

Surface modification, such as coating deposition, is a common technique to control corrosion. For example, degradable polymer coatings like poly-lactic acid (PLA), poly(ε-caprolactone) (PCL), and polyethylene glycol (PEG) have high potential because of their excellent biocompatibility, tunable properties, and drug delivery characteristics [13], but the protection effectiveness is influenced by their own properties. It has been reported that the crystallinity and degradation behavior of polymers significantly influence their protection effectiveness [14–16]. Common PLA coatings have a crystallinity of 30%–50%, and the amorphous region swells after absorbing water, which assist ion diffusion [17–19]. Weakly acidic lactide (LA) is generated in the degradation of PLA, accompanied by the onset of the acidic self-catalytic effect and inflammation [15, 19, 20]. The durability of PLA coating is limited. Polyhydroxybutyrate (PHB) with good biocompatibility is also suitable for anti-corrosion of Mg alloys [21]. Moreover, it has been shown that biodegradable PHB exhibits a 67% lower degradation rate than PLA after six-week immersion, due to its higher crystallinity (60%–80%) [14, 22]. And the main degradation product of PHB, 3-hydroxybutyric acid (3HB), produces lower acidity and inflammation [14, 23]. Therefore, the PHB coating is a promising candidate for durable anti-corrosion of Mg alloys. Moreover, further detailed studies about the influence of crystallinity and degradation behavior on protective behavior are still desired.

The degradation of coated Mg-based stents also depends on the physiological environment. Proteins (60–80 g L^{-1}) are the main organic component in human blood and adsorb on the stent surface after implantation [24]. The protein adsorption layer acts as an ion diffusion barrier [5], consequently inhibiting hydrolysis of the surface coating. The degradation of coatings can also impact protein adsorption and, ultimately, the corrosion behavior of Mg-based stents [25, 26]. In addition, the interactions between proteins and polymer coatings are still not well understood, although it has been shown that protein adsorption is affected by surface properties, such as roughness, surface charge, and wettability [27, 28]. For example, negatively charged BSA in simulated body fluids tends to adsorb more on the positively charged $MgCO_3$ than the negatively charged $CaCO_3$ [28].

In this work, Mg sheet with a thickness (200 μm) similar to that of cardiovascular stents is selected as the research subject for in vitro assessment, in order to better fit the practical application and more accurately reflect the corrosion behavior of stents. PHB and PLA coatings are deposited on Mg sheets to investigate the degradation behavior, corrosion resistance, and blood compatibility, as illustrated in Fig. 1. Our results reveal the important roles of crystallinity and acidic degradation products. The protein–polymer interactions are studied to establish the relationship between the protein concentration and hydrogen evolution.

2 Experimental

2.1 Materials preparation

Pure commercial Mg (99.99%) sheets with a thickness of 200 μm were cut into different sizes according to experimental requirements. They were ground progressively with silicon carbide sandpapers up to 3000#, cleaned ultrasonically in ethanol for 10 min, and dried with warm air. PLA particles and PHB powder were added to dichloromethane (CH_2Cl_2) with a ratio of 0.5 g: 20 mL, respectively. The pre-treated sheets were immersed in the 5 mol L^{-1} sodium hydroxide (NaOH) solution for 25 min, rinsed with deionized water and dried with cold air. The PLA and PHB solutions were dripped onto the alkalized sample surfaces, respectively. Finally, the samples were placed in the oven at 80 °C for 1 h. The coated samples were denoted as A-Mg (with PLA coating) and B-Mg (with PHB coating), respectively.

2.2 In vitro degradation assessment

2.2.1 Hydrogen evolution

Hydrogen evolution was assessed in artificial blood plasma (AP, Table 1) containing different concentrations (0, 1, 3, and 5 g L^{-1}) of bovine serum albumin (BSA) at 37.5 ± 0.5 °C. The dimensions of the coated Mg and bare Mg (control) samples were 2 cm × 2 cm. The samples were placed under a funnel filled with the immersion medium, and the released hydrogen was collected through a centrifugal tube inserted upside down on the funnel. The ratio of the medium volume to the exposed area was 50 mL: 1 cm^2 and the immersion time was 168 h. The volume of hydrogen released and the pH value of the medium were recorded every 2 h. In the experiment, the conditions in the long-term immersion test were the same, and triplicate samples were tested for each condition to improve the statistics. The hydrogen evolution rate (v) was defined as shown in Eq. (1).

$$v = V/(At) \tag{1}$$

where V (mL) is the volume of released hydrogen and A (cm^2) and t (h) are the exposed area and immersion time, respectively.

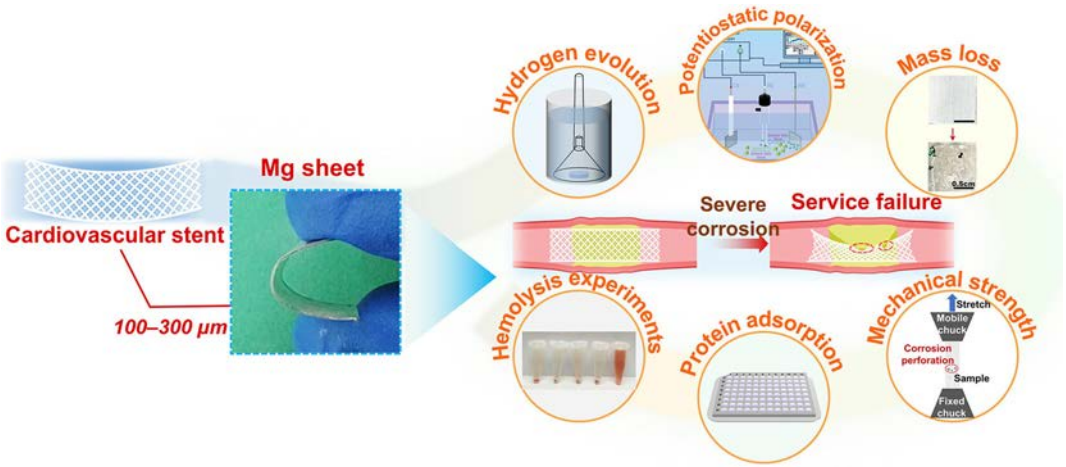

Fig. 1 Schematic illustration of the experimental flow

Table 1 Chemical composition of the AP solution

Reagents	Composition (g L^{-1})
NaCl	6.8
$CaCl_2$	0.2
KCl	0.4
$MgSO_4$	0.1
$NaHCO_3$	2.2
$Na_2HPO_4{\cdot}12H_2O$	0.318
NaH_2PO_4	0.026

2.2.2 Mass loss

The initial mass of the bare Mg was measured before coating deposition. The coating and corrosion products on each sample were washed away with the 200 g L^{-1} chromic acid solution after immersion, and the bare Mg after corrosion was weighed. The mass loss was calculated by the mass reduction per unit area.

2.2.3 Mechanical properties

The corrosion residual strength of Mg, A-Mg, and B-Mg was measured. The sample size was 5 cm × 1 cm × 0.2 mm, and a middle area of 2 cm × 1 cm was exposed to the medium. The coating and corrosion products were washed away from the surface after immersion prior to the tensile test. The uniaxial tension was applied using a displacement-controlled mode at a rate of 1 mm min^{-1}. And the upper limit of the applied force was 100 N. The tensile curves were acquired, and the corrosion residual strength was the tensile strength of the corroded samples.

2.3 Analysis and characterization

2.3.1 BSA concentration

The changes in the BSA concentration in the immersion medium were determined by the bicinchoninic acid (BCA) assay kit. The immersion medium was diluted to 0.25–0.5 mg mL^{-1}, and the medium (20 μL) was added to the 96-well plate. 200 μL of the BCA working liquid was added to each well and incubated at 37 °C for 30 min. The absorbance at 562 nm was measured by a microplate reader (Thermo Scientific MULTISKAN FC), and the BSA concentration in the medium was determined according to the standard curves [29].

2.3.2 Surface characterization

The surface morphology was observed by scanning electron microscopy (SEM, Nova Nano SEM450), and the elemental composition was determined by energy-dispersive X-ray spectrometry (EDS, Oxford Aztec X-Max 80). Fourier transform infrared spectroscopy (FTIR, Nicolet iS10) was performed in the range between 4,000 and 500 cm^{-1}, with an average of 16 scans at a resolution of 4 cm^{-1}. X-ray photoelectron spectroscopy (XPS, Thermofisher Nexsa) was used to analyze the composition and chemical states of the elements in the corrosion products.

2.4 Potentiostatic polarization

Constant potential polarization tests (Chnoampemetry) were performed on the uncorroded Mg, A-Mg, and B-Mg on an electrochemical workstation (Ametek PARSTAT 3000A-DX) based on the standard three-electrode configuration. The sample was the working electrode (WE), and the saturated calomel electrode and Pt were the reference

(RE) and counter (CE) electrodes, respectively. The electrodes were immersed in the AP solution. The polarization voltage was set to + 0.25 V (vs. OC), and the testing time was 600 s. The current–time (*I–t*) curve was recorded, and the surface changes of the samples were observed.

2.5 Hemocompatibility

Table 2 lists the components of the Ca- and Mg-free phosphate buffered saline solution (PBS) used in the hemolysis test. The samples and the consumables were sterilized with ultraviolet light for 5 min before the test. The experiment was carried out according to the standard "ASTM F756-17" [30].

The pH of the Ca- and Mg-free PBS was adjusted to 7.2–7.4. Mg, A-Mg, and B-Mg were immersed in 10 mL of PBS, while 10 mL PBS was the negative control group and 10 mL of ultra-pure water was the positive control. 1 mL of the diluted erythrocyte solution was added to each tube, followed by incubation and centrifugation. The color of the solution was recorded. The supernatant (200 μL) was added to a 96-well plate, and each test was carried out 6 times. Finally, the absorbance at 560 nm was measured on a microplate reader (Thermo Scientific MULTISKAN FC), and the hemolysis rate was calculated as shown in Eq. (2).

$$\text{Hemolysis rate} = \frac{\text{absorbance of experimental sample} - \text{absorbance of negative control}}{\text{absorbance of positive control} - \text{absorbance of negative control}} \times 100\% \quad (2)$$

3 Results

3.1 Hydrogen evolution and characterization

The corrosion resistance of the samples is assessed by in vitro hydrogen evolution. The hydrogen evolution curves of the Mg, A-Mg, and B-Mg during 7-day immersion are shown in Fig. 2A, B. PLA and PHB show different protection in the later immersion stage, which is related to the properties of the polymer coatings. B-Mg has the smallest total hydrogen evolution volume (HEV), which is less than 70% of Mg, after 7-day immersion in the AP solution. However, the total HEV of A-Mg is 0.64466 mL cm^{-2}, while that of Mg is 0.25383 mL cm^{-2} (Fig. 2A1), suggesting that the PLA coating promotes the corrosion of the Mg sheet in the AP solution. The total HEV decreases with BSA concentration, which is related to more adsorption of BSA. Compared to 0 g L^{-1} BSA, the HEV of Mg, A-Mg, and B-Mg decreases by about 65%, 88%, and 75%, respectively, with 5 g L^{-1} BSA (Fig. 2A4). In addition, PLA shows corrosion resistance in the immersion medium containing 3 and 5 g L^{-1} BSA. It can be seen that the BSA concentration shows a more dramatic effect on the corrosion of A-Mg. For the curves of hydrogen evolution rate (HER), the hydrogen evolution of A-Mg exceeds that of Mg after 32 h in AP solution, and eventually reaches a steady state of about 2.5 times of Mg (Fig. 2B1). Although HER follows the order of Mg > A-Mg > B-Mg for 3 and 5 g L^{-1} BSA, the rise in the HER curves of A-Mg around 144 h (Fig. 2C3, C4) implies that the hydrogen evolution of A-Mg exceeds Mg after a long period. The particular corrosion behavior of A-Mg is attributed to the degradation of PLA and protein-PLA interactions. And it can be preliminarily concluded that the PHB coating offers higher durability and better protection in vitro compared to the PLA coating. In addition, the HEV of Mg with a thickness of 4 mm has been shown to stabilize with the immersion time [19]. It is significantly different from the HEV variation of Mg sheets, especially A-Mg (Fig. 2A1, A2) boding well for Mg-based cardiovascular stents in the blood.

The changes in the BSA concentration with time are displayed in Fig. 2D1–D3. The discrepancy between the measured initial concentration and the theoretical value is attributed to experimental errors, which does not affect the analysis of the concentration changes. The concentration of BSA in the media under different conditions reduces dramatically during the initial stages of immersion, which is related to protein adsorption. With the extension of immersion time, the BSA concentration fluctuates due to the adsorption-detachment process on the surface of the sample. The smaller final BSA concentration is attributed to surface adsorption. BSA adsorption increases roughly with the initial BSA concentration in the medium, as shown in Fig. S1. Enhanced adsorption indicates a more complete protein adsorption layer. In addition, under the condition of 1 g L^{-1} BSA, compared with Mg and B-Mg, the adsorption amount of BSA on the surface of A-Mg during the immersion process (72–120 h) is the highest. It implies that more favorable factors for BSA adsorption have appeared on the corroded surface of A-Mg, such as charge, roughness.

The morphology and elemental composition of the corrosion products are shown in Fig. 3. Cracks are observed from the PLA coatings on A-Mg after immersion for 7 days in AP solution, as shown in Fig. 3B1. In

Table 2 Chemical composition of the Ca- and Mg-free PBS

Reagents	Composition (g L^{-1})
NaCl	9.0
$Na_2HPO_4{\cdot}12H_2O$	0.97
KH_2PO_4	0.21

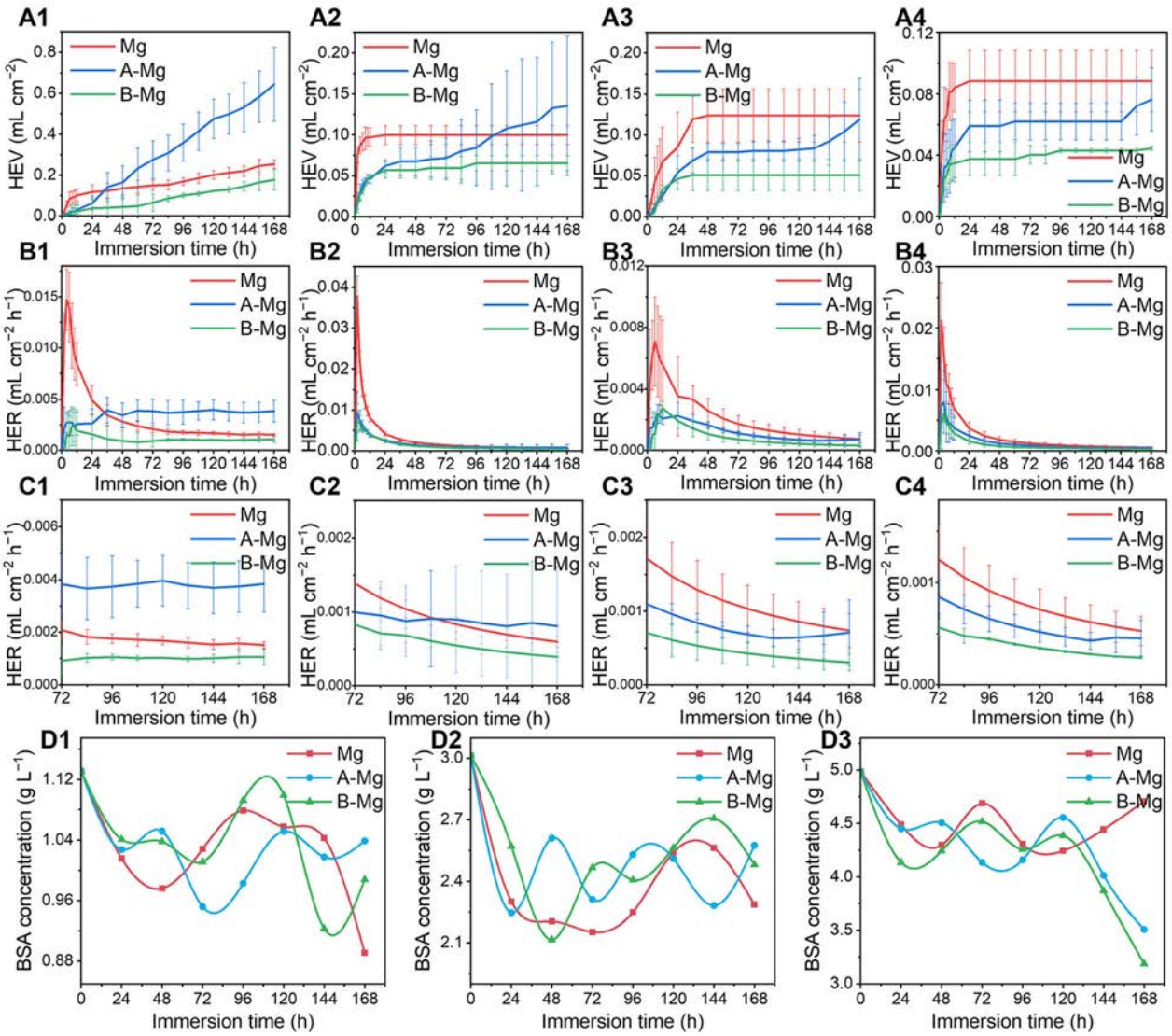

Fig. 2 **A1**–**A4** HEV and **B1**–**B4** HER curves during 7-day immersion in the AP solution with different BSA concentrations: **A1**, **B1** AP + 0 g L^{-1} BSA; **A2**, **B2** AP + 1 g L^{-1} BSA; **A3**, **B3** AP + 3 g L^{-1} BSA; **A4**, **B4** AP + 5 g L^{-1} BSA, **C1**–**C4** are local enlargement of **B1**–**B4**, respectively. Changes in BSA concentration in different media during immersion: **D1** AP + 1 g L^{-1} BSA; **D2** AP + 3 g L^{-1} BSA; **D3** AP + 5 g L^{-1} BSA

comparison, the PHB coatings are more intact without obvious cracks (Fig. 3C1). The distribution of corrosion products is more uniform and denser with increasing BSA concentration to enable better protection. Notably, there is no obvious destruction of the PLA coating for 5 g L^{-1} BSA (Fig. 3B4).

The main element composition of the selected areas in the red boxes in Fig. 3A–C is shown in Fig. 3D1–D3. The main elements of the corrosion product are C, O, Mg, P, and Ca. The Mg salts, such as MgO and $Mg(OH)_2$, are uniformly distributed on the surface, and calcium and phosphorus salts are mostly present as granular deposits. The polymer coating constitutes a carbon source. Compared to Mg and A-Mg, B-Mg has the highest C content under the same condition (Fig. 3D3). However, A-Mg only shows a significant C content for 5 g L^{-1} BSA (Fig. 3D2). The C content is consistent with the morphology, indicating the better durability of PHB during immersion, corrosion inhibition effects of BSA, and significant effects on A-Mg.

The cross-sectional morphology of the samples after corrosion is examined, as shown in Fig. 4. The area between the two yellow dashed lines represents the cross-section in the images. The upper part is the corroded surface which includes the corrosion product and surface coating, and the lower part is the conductive adhesive or

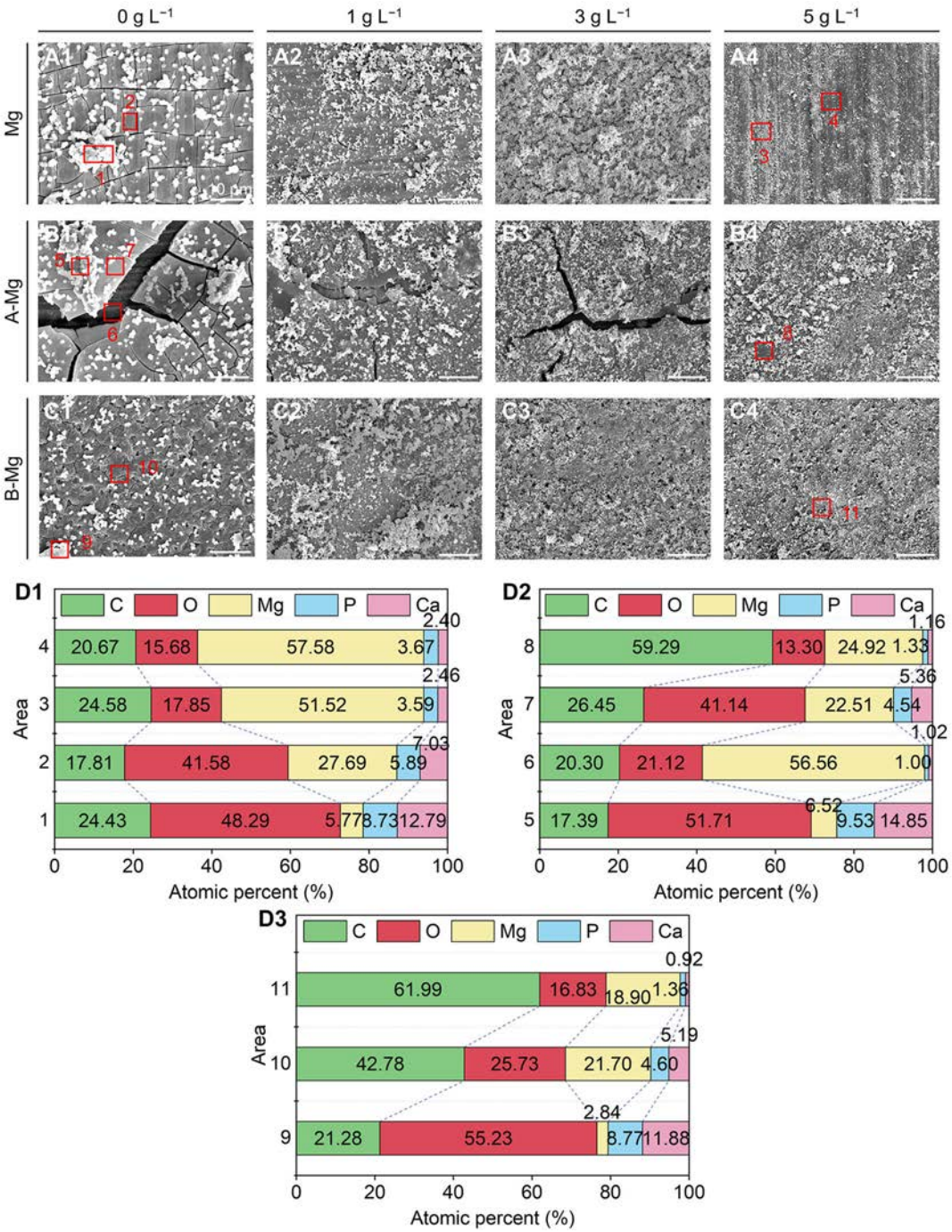

Fig. 3 SEM images of **A1**–**A4** Mg, **B1**–**B4** A-Mg, and **C1**–**C4** B-Mg after 7-day immersion in the AP solution with different BSA concentrations; **D1**–**D3** chemical compositions of the regions marked by red boxes

the back side of the sample. The polymer coatings are clearly observed, as shown by the orange-framed regions in Fig. 4B1–B4 and C1–C4. The cracks and delamination of the PLA coating are shown in Fig. 4B1, B4, and B-Mg shows better intactness of the PHB coating. The red-frame region in Fig. 4A1 shows the typical morphology of corrosion product accumulation by perforation. The EDS maps are displayed in Fig. 4D, and the corrosion products are mainly composed of Mg, C, and O.

The initial macroscopic and corrosion morphologies with corrosion products removed from the surface are displayed in Fig. 5. They directly reflect the extent of corrosion of the three samples in the immersion media, which is consistent with the results of hydrogen evolution.

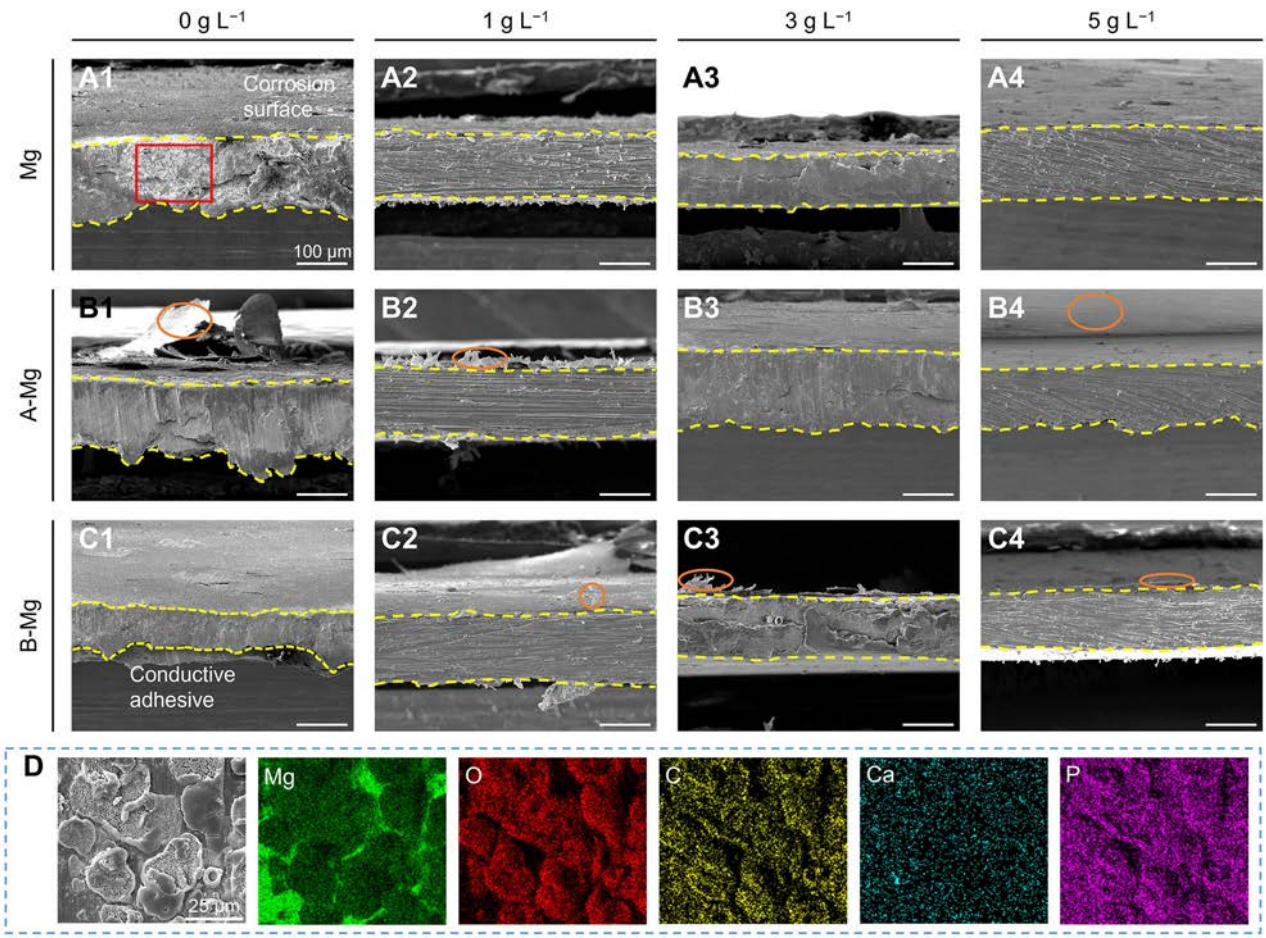

Fig. 4 Cross-sectional morphologies of **A1**–**A4** Mg, **B1**–**B4** A-Mg, and **C1**–**C4** B-Mg after 7-day immersion in the AP solution with different BSA concentrations; **D** EDS maps of the red-frame region in **A1**

The PLA coating and PHB coating initially cover the Mg surface completely. PLA has a higher transparency due to the crystallinity. Corrosion perforation occurs on Mg and A-Mg after immersing in the AP solution for 7 days, as shown in the area marked with the red dashed line (Fig. 5A2, B2). Local corrosion is more serious on A-Mg, while Mg coated with PHB exhibits no perforation after immersion, as shown in Fig. 5C2. The ImageJ software is employed to analyze the morphologies of Mg, A-Mg, and B-Mg, as shown in Fig. 5E2–G2. The black regions represent the corrosion holes, and no perforation occurs in the white regions. The ratio of the area of corrosion holes to the total area follows the order of A-Mg (2.695%) > Mg (0.357%) > B-Mg (0.284%) (Fig. 5D), which demonstrates that PLA and PHB coatings with different properties have a large difference in protection. The corrosion morphology of each sample becomes relatively uniform and is gradually inhibited with increasing BSA concentrations. The change of PLA-coated Mg is more dramatical. A-Mg transitions from extensive perforation (Fig. 5B2) to no perforation (Fig. 5B4), exhibiting lighter corrosion than bare Mg for 3 g L^{-1} BSA.

The XPS spectra of the corrosion products for 3 g L^{-1} BSA are displayed in Figs. 6A–C and S2. The main components of corrosion products are Mg, C, O, Ca, and P based on EDS, and N is detected after adding BSA. The high-resolution XPS spectrum of C 1s exhibits three peaks. The peak at 284.8 eV corresponds to C–C, that from organic C–O is detected at 286.0–286.7 eV, and that at 288.0–290.0 eV stems from CO_3^{2-} and organic C=O [31, 32]. CO_3^{2-} is attributed to carbonate in the corrosion product, consistent with EDS/FTIR. The organic C=O is derived from O=C–N in BSA and O=C–O in PLA/PHB coatings, so there is no C=O peak on the Mg surface without BSA. The organic C–O mainly comes from O=C–O in the coating, which is the location of ester group breakage during the degradation process of the coating.

The XPS spectrum of O 1s contains two peaks. The peak at 532–534 eV (represented as Peak 1) represents organic C=O. The peak at 531–532 eV (Peak 2) is assigned

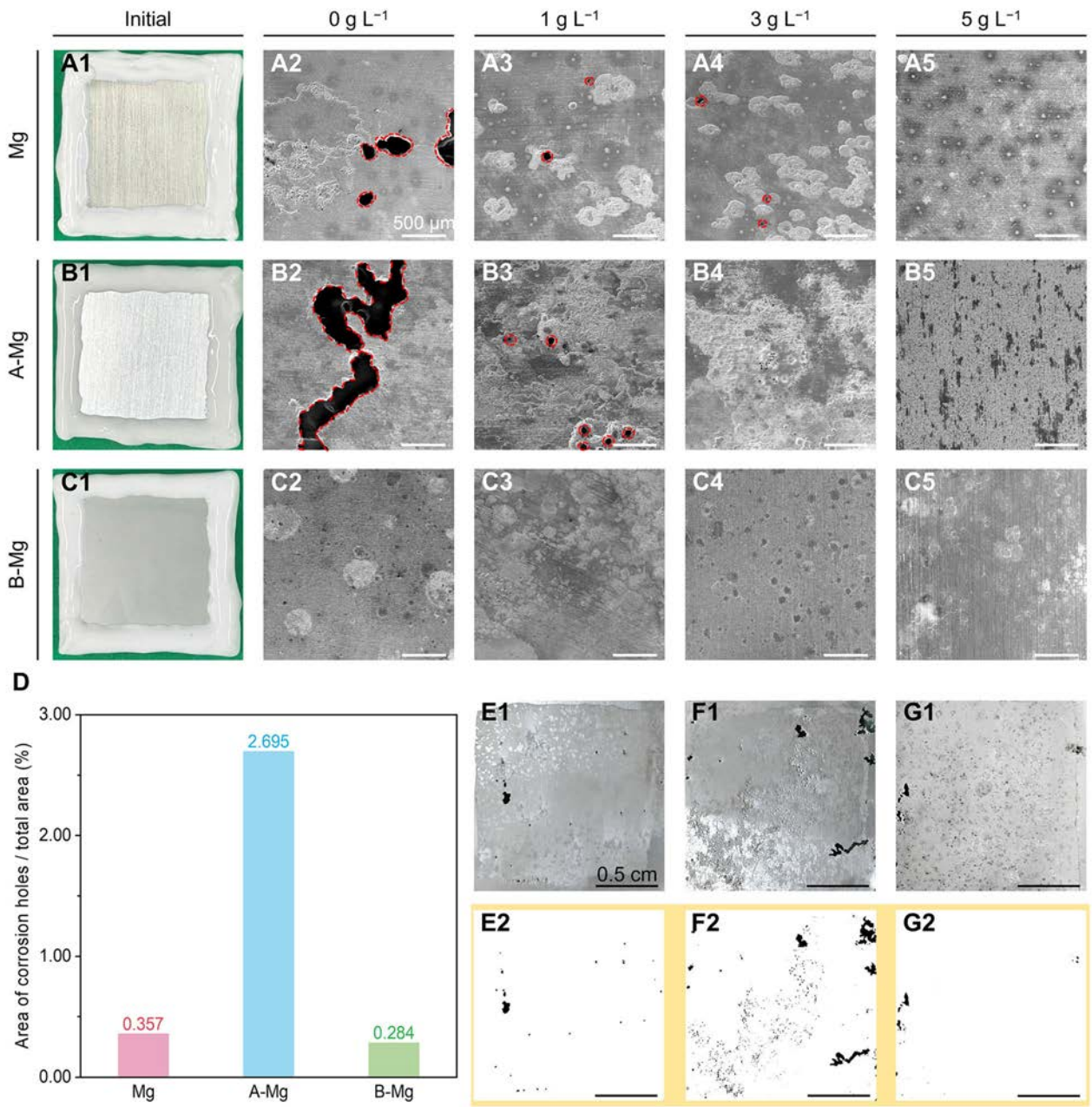

Fig. 5 Initial macroscopic and SEM morphologies after corrosion product removal: **A1**–**A5** Mg, **B1**–**B5** A-Mg, and **C1**–**C5** B-Mg. **D** Ratios of corrosion hole area to total area; image processing of **E1**, **E2** Mg, **F1**, **F2** A-Mg, and **G1**, **G2** B-Mg after corrosion products removal and 7-day immersion in the AP solution

to $Mg(OH)_2$ and CO_3^{2-}, and the organic C–O is also in this range. The area of the two peaks of O 1s under different conditions (in Figs. 6A2–C2 and S3) shows the relative content of the corresponding functional groups (Fig. 6D). The area of Peak 1 of B-Mg is larger than that of A-Mg, maybe due to peeling of the PLA coating. There are more corrosion products and more serious corrosion on A-Mg, in combination with the larger area of Peak 2. The area of Peak 2 of B-Mg is comparable to that of A-Mg, but corrosion on B-Mg is less serious according to hydrogen evolution and SEM morphologies. C–O attributed to the coating also contributes to the area of Peak 2. The relatively complete PHB coating on the surface of Mg sheets may be the reason for the large area of Peak 2, as shown by SEM.

The FTIR spectra of the corrosion product on Mg, A-Mg, and B-Mg immersed in the BSA-containing AP medium for 7 days are shown in Fig. 6E1–E4. The broad

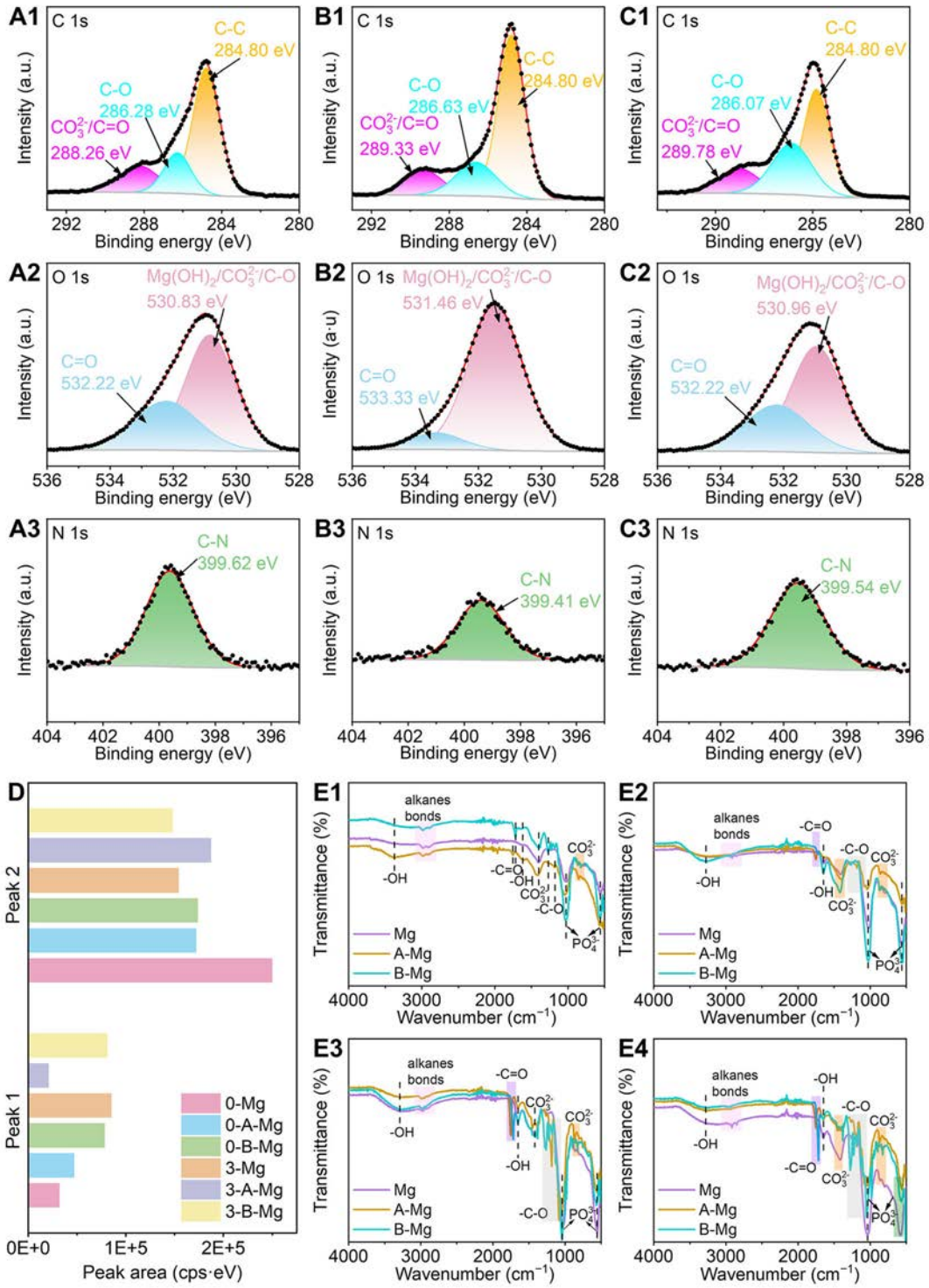

Fig. 6 XPS spectra of **A1**–**A3** Mg, **B1**–**B3** A-Mg, and **C1**–**C3** B-Mg after immersion in the AP + 3 g L^{-1} BSA solution for 7 days; **D** peak areas of the O 1s spectra in **A2**–**C2** and Figure S3. FTIR spectra of the corrosion products on Mg, A-Mg, and B-Mg immersed in AP solutions with different BSA concentrations for 7 days: **E1** AP + 0 g L^{-1} BSA; **E2** AP + 1 g L^{-1} BSA; **E3** AP + 3 g L^{-1} BSA; **E4** AP + 5 g L^{-1} BSA. The vertical coordinate range in the spectra is consistent

band between 3700 and 3000 cm^{-1} represents the stretching vibration of –OH [33]. The peak near 1645 cm^{-1} is attributed to the bending vibration of –OH, and that at 2900–3000 cm^{-1} is assigned to the alkane bonds [32]. The peak at 1715–1760 cm^{-1} corresponds to the stretching of C=O [32], and those at 1180 cm^{-1} of A-Mg and 1274 cm^{-1} of B-Mg represent the stretching of C–O [34, 35]. Alkanes and C=O are derived from BSA and coatings, and C–O mainly comes from the coatings. The peak intensity of C=O and C–O varies with the concentration of BSA and polymer coatings. For example, C=O and C–O bonds are not detected from the surface of Mg immersed in the AP solution. The peak at 1400–1420 cm^{-1} is associated with the asymmetric stretching vibration of CO_3^{2-}, and that at 820–870 cm^{-1} is related to the bending vibration of CO_3^{2-}. The vibrations of PO_4^{3-} bonds can be observed at 1030 and 560 cm^{-1} [31, 32, 36], indicating the presence of carbonate and phosphate in the corrosion products. In summary, the corrosion product is mainly composed of $Mg(OH)_2$, Mg/Ca-HPO_4/PO_4, Ca/$MgCO_3$, and adsorbed BSA.

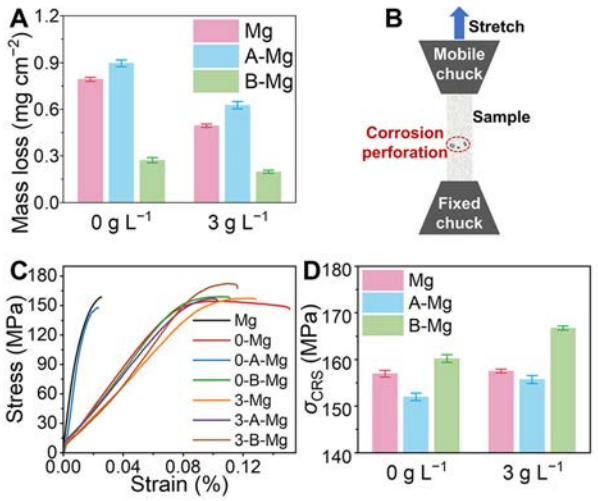

Fig. 7 **A** Mass loss of Mg, A-Mg, and B-Mg in AP + 0/3 g L^{-1} BSA solution after 7-day immersion. **B** Illustration of tensile experiments; **C** tensile curves; **D** the σ_{CRS} of Mg, A-Mg, and B-Mg in the AP + 0/3 g L^{-1} BSA solution after 7-day immersion

3.2 Mass loss and corrosion residual strength

The role of a stent is to expand and support the narrow blood vessels, so its mechanical property is very important, which is related to whether it can achieve the support function as scheduled. However, the stress concentration caused by local corrosion has a significant impact on the mechanical property of the stents. Therefore, Mg sheets with a thickness of 200 μm are selected for immersion tests. The mass loss and corrosion residual strength are determined to investigate the effects of different polymer coatings and BSA concentrations on the corrosion properties of Mg sheets. BSA concentrations of 0 and 3 g L^{-1} are selected in the experiments.

The mass loss of Mg, A-Mg, and B-Mg after immersion in AP + 0/3 g L^{-1} BSA solution for 7 days is displayed in Fig. 7A. The mass loss after corrosion decreases by 37.7% for Mg, 30.1% for A-Mg, and 27.8% for B-Mg as the BSA concentration increases. B-Mg shows the smallest mass loss (< 0.3 mg cm^{-2}) in different media. The mass loss of Mg sheets is reduced by more than 60% with the PHB coating. In contrast, A-Mg shows the largest mass loss, which is nearly 3 times that of B-Mg.

The tensile experiments are illustrated in Fig. 7B. Fracture occurs preferentially in the cross perforation, verifying that severe corrosion critically affects the Mg-based stents. The tensile curves and corrosion residual strength (σ_{CRS}) are presented in Fig. 7C, D. The change of σ_{CRS} is the same as that of the mass loss. The σ_{CRS} value of Mg increases by 0.36% for 3 g L^{-1} BSA, while those of A-Mg and B-Mg increase by 2.45% and 4.09%, respectively. The σ_{CRS} values of A-Mg and bare Mg are comparable for 3 g L^{-1} BSA condition. Moreover, the σ_{CRS} shows the order of B-Mg > Mg > A-Mg for different BSA concentrations (Fig. 7D). The smallest mass loss and largest σ_{CRS} indicate that the PHB coating impedes corrosion of Mg.

3.3 Potentiostatic polarization

Polymer coatings protect Mg by blocking water molecules and corrosive ions through complex molecular structures. The electrochemical polarization test applies an electric field force to Cl^- and Mg^{2+} as the driving force for diffusion (Fig. 8A), which can be used to evaluate the ion barrier ability of PLA and PHB coatings. The changes in the anodic polarization current with time (*I–t* curve) and macroscopic surface morphologies of Mg, A-Mg, and B-Mg are shown in Fig. 8. Corrosion appears on the Mg surface immediately after contact with the medium (Fig. 8C1), as verified by the highest polarization current (42 mA, Fig. 8B1) after applying the voltage. The immersion medium becomes turbid as corrosion accelerates due to the polarization voltage. Corrosion products are deposited on the Mg surface thus preventing the permeation of corrosion ions and further degradation of Mg. As a result, the corrosion current of Mg drops to 34 mA.

A-Mg shows effective corrosion resistance in the early stage with a polarization current of about 2 mA. Small local corrosion sites emerge around 120 s, as shown by the rectangular selected area in Fig. 8C2. However, the PLA coating ruptures at 300 s, and H_2 continues to be generated

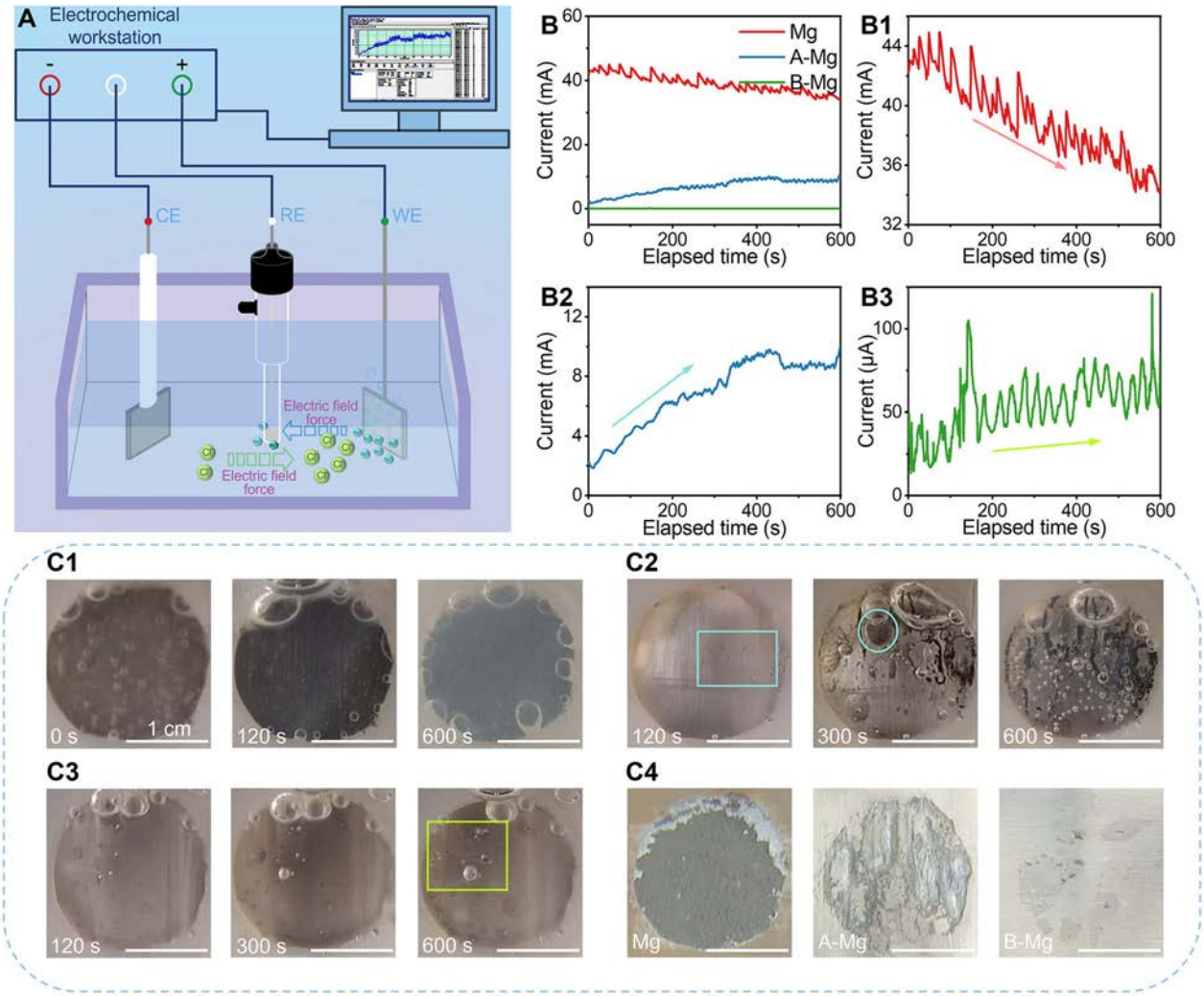

Fig. 8 **A** Illustration of the electrochemical assessment setup; **B** *I*–*t* curves of the samples in the AP solution at a constant potential of + 0.25 V, and **B1**–**B3** are magnified curves of Mg, A-Mg, and B-Mg, respectively. Macroscopic morphological changes during polarization of **C1** Mg, **C2** A-Mg, and **C3** B-Mg; **C4** final morphologies

at the PLA-Mg interface (circular area in Fig. 8C2). Finally, the PLA coating delaminates partially to expose the Mg surface (Fig. 8C2). Severe corrosion on A-Mg is indicated by the increase in the *I*–*t* curve, and the current eventually stabilizes at about 9 mA (Fig. 8B2). The change in current directly reflects the gradual weakening of the barrier effect of the PLA coating against ion diffusion, which is related to the hydrolysis of PLA. In turn, the hydrolysis is attributed to the diffusion of water molecules and corrosive ions within the coating.

Compared with Mg and A-Mg, the corrosion current of B-Mg is the smallest. Some local corrosion sites appear during polarization, but there is no extensive and serious surface damage in the PHB coating (the rectangular selected area in Fig. 8C3). The *I*–*t* curve of B-Mg is relatively flat with the current being stable between 50 and 75 μA, as shown in Fig. 8B3. It suggests that PHB can stably block the diffusion of ions, even when driven by an electric field. Throughout the entire test, the corrosion current shows the order of Mg > A-Mg > B-Mg. B-Mg has the lowest electrochemical reactivity, and the morphology of PHB coating is more complete after destruction (Fig. 8C4). It implies that the PHB coating blocks corrosive ions more effectively, has better durability and provides more protection than the PLA coating.

3.4 Blood compatibility in vitro

The coatings on the surface of cardiovascular stents are in direct contact with blood. Therefore, in addition to the anti-corrosion performance, blood compatibility is also assessed in vitro. The hemolytic properties of Mg, A-Mg, and B-Mg

are presented in Fig. 9. The plasma corresponding to the three experimental samples is light red, and the precipitated erythrocyte and plasma are separated. All the samples have good blood compatibility as shown by the acceptable hemolysis range (< 5%). The hemolysis rate shows the order of Mg > A-Mg > B-Mg, disclosing that the PLA and PHB coatings improve the blood compatibility of bare-Mg, while the PHB coating has the best effect.

4 Discussion

The protection effectiveness of the PLA and PHB coatings in the BSA-containing AP solution is evaluated and compared. The HEV of Mg sheets increases by 154% with the PLA coating for 0 g L^{-1} BSA, while PHB reduces the HEV by at least 30%. The polarization results also show that the PHB coating provides more effective and stable protection. In addition, higher BSA concentrations inhibit corrosion. The corrosion behavior of A-Mg is influenced the most by the BSA concentration. However, the structure–property–performance relationship and the interactions between proteins and polymer coatings must be systematically analyzed in order to establish the relationship between the BSA concentration and hydrogen evolution.

4.1 Molecular structure, properties, and anti-corrosion characteristics of polymer coatings

Corrosion occurs when water molecules and corrosive ions come in contact with the Mg substrate. The polymer coating acts as a physical barrier to mitigate permeation. However, water molecules (H_2O) and ions (in the form of hydrated ions) can diffuse through amorphous regions in the coating due to the concentration gradient [19, 37]. The process of permeation of H_2O and corrosive ions is shown in Fig. 10A1, A2. H_2O with the smallest size first reaches the coating-Mg interface to form a $Mg(OH)_2$ layer. The polymer gradually hydrolyzes, and corrosive Cl^- with a smaller hydrated radius and larger concentration diffuses to the interface to damage the $Mg(OH)_2$ layer and aggravate corrosion. Diffusion of H_2O and Cl^- leads to serious hydrolysis of the polymer, consequently allowing more water molecules, anions, and cations to permeate the coating [15, 34]. Therefore, the protection efficiency is significantly impacted by the molecular structure and degradation characteristics of the polymer.

Compared to PLA, PHB is isotactic, with all the chiral carbon atoms at the same position. Hence, PHB has higher crystallinity than PLA. Polymers with higher crystallinity can prevent ion permeation and reduce the corrosion rate (Fig. 10A1, A2) [17, 19]. Furthermore, PLA swells after absorbing water to weaken the interactions between molecular chains, reduce the resistance of ion permeation, and accelerate the hydrolysis of PLA and corrosion of Mg.

The degradation products of PLA and PHB are LA and 3HB, respectively, and their molecular structures are shown in Fig. 10B1, B2. There is an extra methylene group ($–CH_2$) between the hydroxyl group (–OH) and carboxylic group (–COOH) in 3HB. The closer –OH is to –COOH, the lower the charge density of O in –O–H in –COOH, thus making H^+ dissociation easier. Therefore, LA is more acidic than 3HB, and the degradation of PLA decreases the local pH making the dissolution of Mg easier. PLA degrades more severely due to the acidic self-catalytic effect [2, 20]. The higher crystallinity, less acidic degradation products, and uncatalyzed hydrolysis explain why PHB delivers better anti-corrosion performance than PLA.

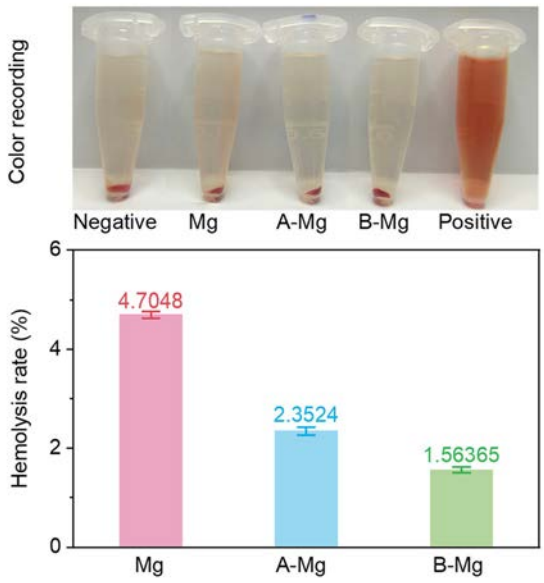

Fig. 9 Hemolytic properties of Mg, A-Mg, and B-Mg

4.2 Protein-polymer interactions and effects of protein concentrations on corrosion

Degradation of the polymer coating, corrosion of Mg, and BSA adsorption occur during immersion. The first two processes are influenced by BSA adsorption, and the surface properties of the coating or Mg (roughness, density of the product layer, surface charge, etc.) dictate the BSA-surface interaction [28].

The interaction between BSA and Mg during immersion is shown in Fig. 10C1. $Mg(OH)_2$ is formed on the surface as soon as the bare Mg comes in contact with the medium, and the surface roughness increases. $Mg(OH)_2$ (isoelectric point (PI): 10.8–14 [38], pH < PI) is positively charged and attracts negatively charged BSA (PI: 4.7–5.2 [39],

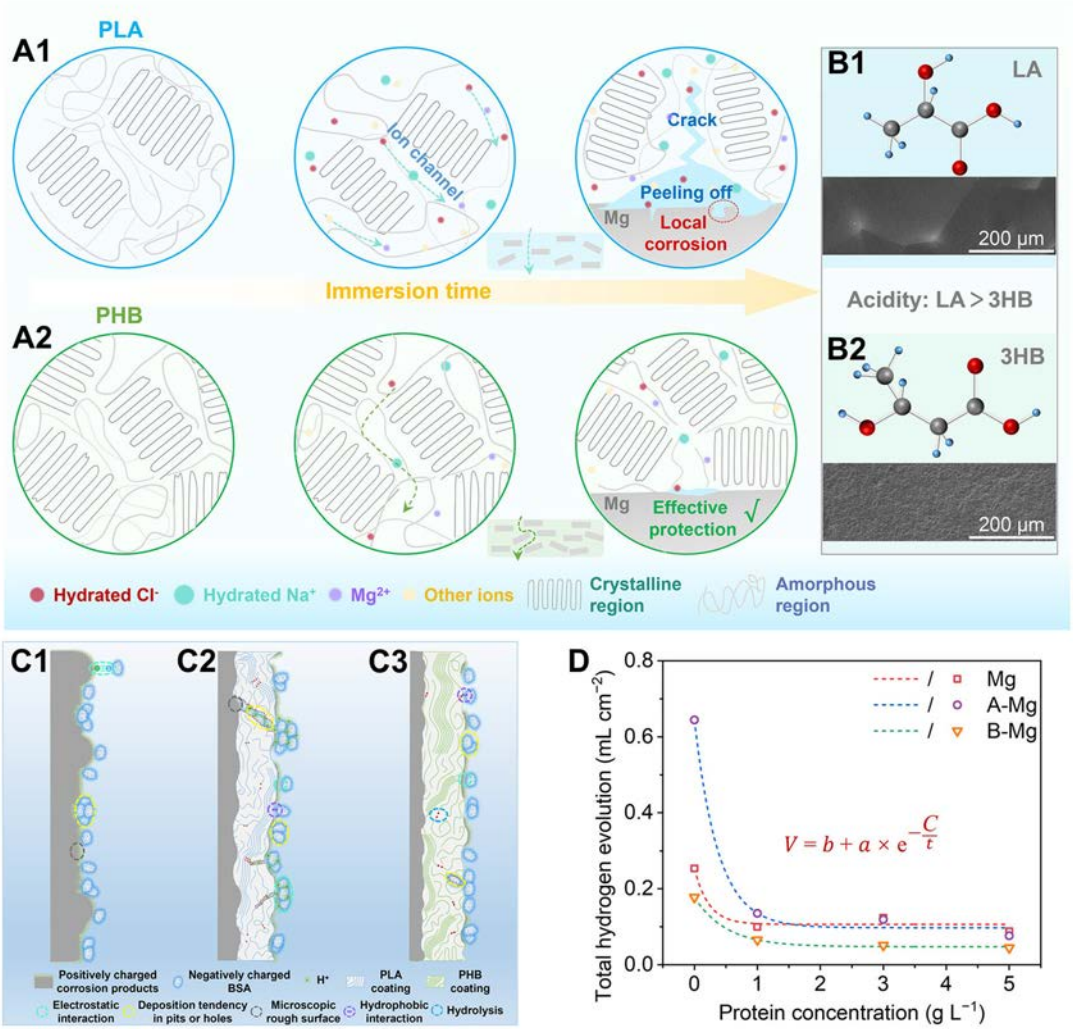

Fig. 10 Schematic diagrams illustrating ion permeation through **A1** PLA and **A2** PHB coatings on the molecular scale. Molecular structure and surface morphology of **B1** LA and **B2** 3HB. Schematic diagrams illustrating BSA adsorption on **C1** Mg, **C2** A-Mg, and **C3** B-Mg on the molecular scale. **D** Fitted curves of hydrogen evolution versus protein concentration of Mg, A-Mg, and B-Mg

pH > PI). BSA also tends to adsorb around pits. The combined effects lead to quick adsorption of BSA onto the Mg surface to form a protective layer, which covers the electrochemically active surface sites and blocks corrosive ions [40, 41]. The interaction between BSA and PLA-coated Mg during immersion is shown in Fig. 10C2. A large amount of H^+ generated by local hydrolysis of PLA attracts BSA electrostatically. The maximum adsorption capacity of BSA is close to the PI point [28]. Therefore, the adsorption of BSA on PLA is mainly attributed to the acidic degradation products. The slightly hydrophobic surface of PLA and exposed corroded Mg also attract BSA. As for B-Mg (Fig. 10C3), it mainly attracts BSA due to its hydrophobicity and slightly larger roughness (Fig. 10B2).

According to the hydrogen evolution results, the relationship between the amount of protein in the medium and the total HEV of Mg, A-Mg, and B-Mg can be expressed by Eqs. (3–5) (Fig. 10D):

$$V_1 = 0.1064 + 0.1472 \times e^{-\frac{C}{0.2286}} (R^2 = 0.95998) \quad (3)$$

$$V_2 = 0.0975 + 0.5472 \times e^{-\frac{C}{0.3763}} (R^2 = 0.99580) \quad (4)$$

$$V_3 = 0.0474 + 0.1302 \times e^{-\frac{C}{0.5066}} (R^2 = 0.99838) \quad (5)$$

where V_1, V_2, and V_3 are the total HEV (mL cm^{-2}) of Mg, A-Mg, and B-Mg, respectively, and C is the BSA concentration (g L^{-1}) added to the medium.

According to Fig. 10D, corrosion is inhibited as the BSA concentration increases due to a more complete protein adsorption layer [40]. It can also be inferred that a larger density of BSA around pits can prevent the "anisotropic" evolution of corrosion, resulting in a uniform

corrosion rate across the surface [26]. The total HEV tends to be stable at high BSA concentrations. The slope of the curve of A-Mg (0.5472) is the largest, whereas the slopes of M (0.1472) and B-Mg (0.1302) are relatively small. The acidic degradation products of PLA promote BSA adsorption. The BSA layer exhibits the ion barrier and pH buffering effects, which effectively inhibit the hydrolysis of PLA and corrosion of Mg compared with no BSA. Therefore, the BSA concentration has a large impact on the corrosion of A-Mg. The corrosion product layer on the Mg surface has a protective effect, and the PHB coating is an extremely effective diffusion barrier, which is different from the corrosion-promotion effect of PLA in the AP solution. As a result, the BSA concentration and BSA adsorption have a smaller influence for Mg and B-Mg.

5 Conclusion

In this study, PHB coatings are prepared on Mg sheets, and the protection capability in different BSA-containing media is determined and compared with those of PLA coatings. The hydrogen evolution volume decreases by 30% in the AP solution after 7-day immersion due to the PHB coating, while that coated with PLA shows an increase of 154%. Furthermore, compared with PLA-coated Mg, the PHB-coated Mg has the higher corrosion residual strength, better durability at a constant polarization voltage, and blood compatibility. The PHB layer blocks corrosive ions because of higher crystallinity than PLA. The limited protection of PLA is also attributed to the acidic degradation products, acidic self-catalytic effect, and swelling. Moreover, BSA adsorption leads to the formation of a surface layer due to electrostatic attraction and hydrophobic interaction. A more complete physical barrier is formed at a higher concentration. And BSA tends to accumulate around corrosion pits to form a high-density zone and make corrosion more uniform. Therefore, corrosion is inhibited as the BSA concentration increases. Compared with the BSA-free condition, the hydrogen evolution volume of Mg, PLA-coated Mg, and PHB-coated Mg decreases by 65%, 88%, and 75%, respectively, for 5 g L^{-1} BSA. The effect of PLA on the corrosion of Mg changes from promotion to inhibition at high protein concentration.

Acknowledgements This work was jointly supported by the National Natural Science Foundation of China (No. 52171236), State Key Program of the National Natural Science Foundation of China (No. 52231005), Open Research Fund of Jiangsu Key Laboratory for Advanced Metallic Materials, Southeast University (No. AMM2024A01), Suzhou Science and Technology Project (Nos. SJC2023005 and SZS2023023), City University of Hong Kong Donation Research Grants (Nos. DON-RMG 9229021 and 9220061), Hong Kong Innovation and Technology Fund (Nos. ITF GHP/212/22GD and CityU 440399), Hong Kong PDFS_RGC Postdoctoral Fellowship Scheme (Nos. PDFS2122-1S08 and CityU 9061014), and Hong Kong HMRF (Health and Medical Research Fund) (Nos. 2120972 and CityU 9211320).

Author contributions Bi-Wei Sun: Investigation; methodology; data curation; formal analysis; writing original draft. Ju-Yi Yang: Conceptualization; investigation; methodology; writing—review & editing. Jian-Wei Dai: Data curation; methodology; writing—review & editing. Yan-Bin Zhao: Formal analysis; writing—review & editing. Lu Zhang: Data curation; methodology; writing—review & editing. Zi-Jian Huang: Methodology; writing—review & editing. Jing Bai: Methodology. Feng Xue: Methodology. Paul K. Chu: Writing—review & editing. Cheng-Lin Chu: Conceptualization; funding acquisition; methodology; writing—review & editing.

Data availability The data that support the findings of this study are available from the corresponding author upon reasonable request.

Declarations

Conflict of interests The authors declare that they have no conflict of interest.

References

[1] Zhang ZQ, Yang YX, Li JA, Zeng RC, Guan SK. Advances in coatings on magnesium alloys for cardiovascular stents - a review. Bioact Mater. 2021;6(12):4729. https://doi.org/10.1016/j.bioactmat.2021.04.044.

[2] Hu TZ, Yang C, Lin S, Yu QS, Wang GX. Biodegradable stents for coronary artery disease treatment: recent advances and future perspectives. Mat Sci Eng C-Mater Biol Appl. 2018;91:163. https://doi.org/10.1016/j.msec.2018.04.100.

[3] Fu JY, Su YC, Qin YX, Zheng YF, Wang YD, Zhu DH. Evolution of metallic cardiovascular stent materials: a comparative study among stainless steel, magnesium and zinc. Biomaterials. 2020;230:119641. https://doi.org/10.1016/j.biomaterials.2019.119641.

[4] Qi PK, Yang Y, Maitz FM, Huang N. Current status of research and application in vascular stents. Chinese Sci Bull. 2013;58(35):4362. https://doi.org/10.1007/s11434-013-6070-1.

[5] Yan W, Lian YJ, Zhang ZY, Zeng MQ, Zhang ZQ, Yin ZZ, Cui LY, Zeng RC. In vitro degradation of pure magnesium-the synergetic influences of glucose and albumin. Bioact Mater. 2020;5(2):318. https://doi.org/10.1016/j.bioactmat.2020.02.015.

[6] Bennett J, De Hemptinne Q, McCutcheon K. Magmaris resorbable magnesium scaffold for the treatment of coronary heart disease: overview of its safety and efficacy. Expert Rev Med Devic. 2019;16(9):757. https://doi.org/10.1080/17434440.2019.1649133.

[7] Pan CJ, Liu XH, Hong QX, Chen J, Cheng YX, Zhang QY, Meng LJ, Dai J, Yang ZM, Wang LR. Recent advances in surface endothelialization of the magnesium alloy stent materials. J Magnes Alloy. 2023;11(1):48. https://doi.org/10.1016/j.jma.2022.12.017.

[8] Huang L, Su K, Zheng YF, Yeung KWK, Liu XM. Construction of TiO_2/silane nanofilm on AZ31 magnesium alloy for controlled degradability and enhanced biocompatibility. Rare Met. 2019;38(6):588. https://doi.org/10.1007/s12598-018-1187-7.

[9] Wang Q, Liu YH, Zhu XY, Li SQ, Yu SR, Zhang LN, Song YL. Study on the effect of corrosion on the tensile properties of the 1.0 wt% Yttrium modified AZ91 magnesium alloy. Mat Sci Eng

A-Struct. 2009;517(1):239. https://doi.org/10.1016/j.msea.2009.03.053.
[10] Anjum MJ, Zhao JM, Asl VZ, Malik MU, Yasin G, Khan WQ. Green corrosion inhibitors intercalated Mg: Al layered double hydroxide coatings to protect Mg alloy. Rare Met. 2021;40(8):2254. https://doi.org/10.1007/s12598-020-01538-7.
[11] Zhang M, Deng WL, Yang XN, Wang YK, Zhang XY, Hang RQ, Deng KK, Huang XB. In vitro biodegradability of Mg-2Gd-*x*Zn alloys with different Zn contents and solution treatments. Rare Met. 2019;38(7):620. https://doi.org/10.1007/s12598-019-01220-7.
[12] Seguchi M, Aytekin A, Lenz T, Nicol P, Alvarez-Covarrubias HA, Xhepa E, Klosterman GR, Beele A, Sabic E, Utsch L, Alyaqoob A, Joner M. Challenges of the newer generation of resorbable magnesium scaffolds: lessons from failure mechanisms of the past generation. J Cardiol. 2023;81(2):179. https://doi.org/10.1016/j.jjcc.2022.09.003.
[13] Li LY, Cui LY, Zeng RC, Li SQ, Chen XB, Zheng YF, Kannan MB. Advances in functionalized polymer coatings on biodegradable magnesium alloys - a review. Acta Biomater. 2018;79:23. https://doi.org/10.1016/j.actbio.2018.08.030.
[14] Zhuikov VA, Akoulina EA, Chesnokova DV, You WH, Makhina TK, Demyanova IV, Zhuikova YV, Voinova VV, Belishev NV, Surmenev RA, Surmeneva MA, Bonartseva GA, Shaitan KV, Bonartsev AP. The growth of 3T3 fibroblasts on PHB, PLA and PHB/PLA blend films at different stages of their biodegradation in vitro. Polymers. 2021;13(1):108. https://doi.org/10.3390/polym13010108.
[15] Zeng RC, Cui LY, Jiang K, Liu R, Zhao BD, Zheng YF. In vitro corrosion and cytocompatibility of a microarc oxidation coating and poly(L-lactic acid) composite coating on Mg-1Li-1Ca alloy for orthopedic implants. Acs Appl Mater Interfaces. 2016;8(15):10014. https://doi.org/10.1021/acsami.6b00527.
[16] Liu YN, Liu HF, Yuan DL, Chen SY, Zhu CJ, Chen KH. The effect of polylactic acid ordering on the long-term corrosion protection capacity of biodegradable magnesium alloys. Int J Biol Macromol. 2024;282:135549. https://doi.org/10.1016/j.ijbiomac.2024.135549.
[17] Reddy MSB, Ponnamma D, Choudhary R, Sadasivuni KK. A comparative review of natural and synthetic biopolymer composite scaffolds. Polymers. 2021;13(7):1105. https://doi.org/10.3390/polym13071105.
[18] Tsuji H, Ikada Y. Properties and morphology of poly(L-lactide) 4. Effects of structural parameters on long-term hydrolysis of poly(L-lactide) in phosphate-buffered solution. Polym Degrad Stabil. 2000;67(1):179. https://doi.org/10.1016/S0141-3910(99)00111-1.
[19] Yang JY, Sun BW, Dai JW, Li X, Zhao YB, Zhang L, Bai J, Xue F, Chu CL. Design and fabrication of durable poly(3-hydroxybutyrate) (PHB) coating with high adhesion and desirable anti-corrosion performance on Mg alloy for bio-application. Prog Org Coat. 2024;194:108577. https://doi.org/10.1016/j.porgcoat.2024.108577.
[20] Zhou ZH, Liu XP, Liu QQ, Liu LH. Morphology, molecular mass changes, and degradation mechanism of poly-L-Lactide in phosphate-buffered solution. Polym-Plast Technol. 2009;48(2):115. https://doi.org/10.1080/03602550802497206.
[21] Ma XL, Lv YR, Gao ZX, Cheng GX. Surface modification of biomedical magnesium alloys by PHB. Adv Superalloys. 2010;146–147:1170. https://doi.org/10.4028/www.scientific.net/AMR.146-147.1170.
[22] Anjum A, Zuber M, Zia KM, Noreen A, Anjum MN, Tabasum S. Microbial production of polyhydroxyalkanoates (PHAs) and its copolymers: a review of recent advancements. Int J Biol Macromol. 2016;89:161. https://doi.org/10.1016/j.ijbiomac.2016.04.069.
[23] Ben Abdeladhim R, Reis JA, Vieira AM, de Almeida CD. Polyhydroxyalkanoates: medical applications and potential for use in dentistry. Materials. 2024;17(22):5415. https://doi.org/10.3390/ma17225415.
[24] Yang L, Hort N, Willumeit R, Feyerabend F. Effects of corrosion environment and proteins on magnesium corrosion. Corros Eng Sci Techn. 2012;47(5):335. https://doi.org/10.1179/1743278212y.0000000024.
[25] Wan P, Lin X, Tan LL, Li LG, Li WR, Yang K. Influence of albumin and inorganic ions on electrochemical corrosion behavior of plasma electrolytic oxidation coated magnesium for surgical implants. Appl Surf Sci. 2013;282:186. https://doi.org/10.1016/j.apsusc.2013.05.100.
[26] Wang YS, Lim CS, Lim CV, Yong MS, Teo EK, Moh LN. In vitro degradation behavior of M1A magnesium alloy in protein-containing simulated body fluid. Mat Sci Eng C-Mater Biol Appl. 2011;31(3):579. https://doi.org/10.1016/j.msec.2010.11.017.
[27] Höhn S, Virtanen S, Boccaccini AR. Protein adsorption on magnesium and its alloys: a review. Appl Surf Sci. 2019;464:212. https://doi.org/10.1016/j.apsusc.2018.08.173.
[28] Hou RQ, Willumeit-Romer R, Garamus VM, Frant M, Koll J, Feyerabenet F. Adsorption of proteins on degradable magnesium–which factors are relevant? Acs Appl Mater Interfaces. 2018;10(49):42175. https://doi.org/10.1021/acsami.8b17507.
[29] Han LY, Chu CL, Zhang L, Zhang X, Chen JE, Dai JW, Bai J, Huang ZH, Guo C, Xue F. Effects of different concentrations of BSA on in vitro corrosion behavior of pure zinc in artificial plasma. Acs Biomater-Sci Eng. 2022;8(10):4365. https://doi.org/10.1021/acsbiomaterials.2c00894.
[30] ASTM International. ASTM Standard F756-17: standard practice for assessment of hemolytic properties of materials. ASTM International. 2017. https://doi.org/10.1520/F0756-17
[31] Zhao YB, He P, Yao JY, Li M, Wang B, Han LY, Huang ZH, Guo C, Bai J, Xue F, Cong Y, Cai WH, Chu PK, Chu CL. pH/NIR-responsive and self-healing coatings with bacteria killing, osteogenesis, and angiogenesis performances on magnesium alloy. Biomaterials. 2023;301:122237. https://doi.org/10.1016/j.biomaterials.2023.122237.
[32] Dai JW, Yang JY, Zhang XG, Zhang L, Sun BW, Li X, Bai J, Xue F, Chu CL. Synergistic effects of BSA adsorption and shear stress on corrosion behaviors of WE43 alloy under simulated physiological flow field. Corros Sci. 2024;237:112317. https://doi.org/10.1016/j.corsci.2024.112317.
[33] Zhang L, Zhang X, Dai JW, Yang JY, Huang ZJ, Huang ZH, Guo C, Bai J, Xue F, Han LY, Chu CL. Effects of compressive stress on the corrosion behavior of biodegradable zinc with tension-compression asymmetry under simulated physiological environment. Corros Sci. 2025;242:112566. https://doi.org/10.1016/j.corsci.2024.112566.
[34] Dai JW, Wu CQ, Yang JY, Zhang L, Dong QS, Han LY, Li X, Bai J, Xue F, Chu PK, Chu CL. Poly-lactic acid coatings on the biomedical WE43 Mg alloy: protection mechanism and ion permeation effects. Prog Org Coat. 2023;177:107427. https://doi.org/10.1016/j.porgcoat.2023.107427.
[35] Hagagy N, Saddiq AAN, Tag HM, Abdelgawad H, Selim S. Characterization of bioplastics produced by haloarchaeon Haloarcula sp strain NRS20 using cost-effective carbon sources. Mater Res Express. 2021;8(10):105404. https://doi.org/10.1088/2053-1591/ac3166.
[36] Yang JY, Zhao YB, Dai JW, Han LY, Dong QS, Zhang L, Bai J, Xue F, Chu PK, Chu CL. Fabrication and growth mechanism of multilayered hydroxyapatite/organic composite coatings on the WE43 magnesium alloy. Surf Coat Tech. 2023;452:129125. https://doi.org/10.1016/j.surfcoat.2022.129125.

[37] Tsuji H, Mizuno A, Ikada Y. Properties and morphology of poly(L-lactide). III. Effects of initial crystallinity on long-term in vitro hydrolysis of high molecular weight poly(L-lactide) film in phosphate-buffered solution. J Appl Polym Sci. 2000;77(7):1452. https://doi.org/10.1002/1097-4628(20000815)77:7%3C1452::AID-APP7%3E3.0.CO;2-S

[38] Kosmulski M. Compilation of PZC and IEP of sparingly soluble metal oxides and hydroxides from literature. Adv Colloid Interfac. 2009;152(1–2):14. https://doi.org/10.1016/j.cis.2009.08.003.

[39] Hou RQ, Scharnagl N, Willumeit-Römer R, Feyerabend F. Different effects of single protein vs. protein mixtures on magnesium degradation under cell culture conditions. Acta Biomater. 2019;98:256. https://doi.org/10.1016/j.actbio.2019.02.013.

[40] Wagener V, Faltz AS, Killian MS, Schmuki P, Virtanen S. Protein interactions with corroding metal surfaces: comparison of Mg and Fe. Faraday Discuss. 2015;180:347. https://doi.org/10.1039/C4FD00253A.

[41] Heakal FET, Bakry AM. Serum albumin can influence magnesium alloy degradation in simulated blood plasma for cardiovascular stenting. Mater Chem Phys. 2018;220:35. https://doi.org/10.1016/j.matchemphys.2018.08.060.